The C^{18}O core mass function toward Orion A: Single-dish observations

Hideaki TAKEMURA [iD],[1,2,*] Fumitaka NAKAMURA [iD],[1,2,3] Shun ISHII [iD],[1,2]
Yoshito SHIMAJIRI [iD],[2] Patricio SANHUEZA [iD],[1,2] Takashi TSUKAGOSHI [iD],[2]
Ryohei KAWABE [iD],[1,2] Tomoya HIROTA [iD],[1,2] and Akimasa KATAOKA [iD][1,2]

[1]The Graduate University for Advanced Studies (SOKENDAI), 2-21-1 Osawa, Mitaka, Tokyo 181-0015, Japan
[2]National Astronomical Observatory of Japan, 2-21-1 Osawa, Mitaka, Tokyo 181-8588, Japan
[3]Department of Astronomy, The University of Tokyo, 7-3-1 Hongo, Bunkyo, Tokyo 113-0033, Japan

*E-mail: hideaki.takemura@grad.nao.ac.jp

Abstract

We have performed an unbiased dense core survey toward the Orion A Giant Molecular Cloud in the C^{18}O ($J = 1$–0) emission line taken with the Nobeyama Radio Observatory (NRO) 45 m telescope. The effective angular resolution of the map is 26″, which corresponds to ∼0.05 pc at a distance of 414 pc. By using the Herschel–Planck H$_2$ column density map, we calculate the C^{18}O fractional abundance and find that it is roughly constant over the column density range of ≲5×10^{22} cm^{-3}, although a trend of C^{18}O depletion is determined toward higher column density. Therefore, C^{18}O intensity can follow the cloud structure reasonably well. The mean C^{18}O abundance in Orion A is estimated to be 5.7×10^{-7}, which is about three times larger than the fiducial value. We identified 746 C^{18}O cores with `astrodendro` and classified 709 cores as starless cores. We compute the core masses by decomposing the Herschel–Planck dust column density using the relative proportions of the C^{18}O integrated intensities of line-of-sight components. Applying this procedure, we attempt to remove the contribution of the background emission, i.e., the ambient gas outside the cores. Then, we derived mass function for starless cores and found that it resembles the stellar initial mass function (IMF). The CMF for starless cores, dN/dM, is fitted with a power-law relation of M^{α} with a power index of $\alpha = -2.25 \pm 0.16$ at the high-mass slope (≳$0.44\,M_{\odot}$). We also found that the ratio of each core mass to the total mass integrated along the line of sight is significantly large. Therefore, in the previous studies, the core masses derived from the dust image are likely to be overestimated by at least a factor of a few. Accordingly, such previous studies may underestimate the star formation efficiency of individual cores.

Key words: ISM: clouds — ISM: molecules — stars: formation

1 Introduction

Stars are formed in dense cores embedded in molecular clouds. Therefore, it is important to understand how dense cores form from parental molecular clouds. Previous studies of nearby low-mass star-forming regions have suggested

that a typical dense core has a mass of 1–10 $M_{\odot}$, size of 0.01–0.1 pc, and density of 10^{4-5} cm^{-3} (Bergin & Tafalla 2007). Since the evolutionary processes of stars are partly determined by their masses at birth, it is important to reveal the origin of the mass distribution of dense cores in

molecular clouds. Thus, the mass functions of dense cores (core mass functions; CMFs) are expected to imprint some information on their formation and evolution processes. Salpeter (1955) derived the stellar initial mass function (IMF) for nearby stars and discovered that the IMF has a power-law shape of $dN/dM \propto M^{-2.35}$ at the high-mass end ($\gtrsim 1 \, M_{\odot}$).

Both the CMF and IMF are often characterized by their slopes at the high-mass ends ($\gtrsim 1 \, M_{\odot}$) and the turnover masses at the low-mass part of the distributions. Many previous studies toward nearby star-forming regions have suggested that the CMF has a Salpeter-like slope at the high-mass end and resembles the IMF (Motte et al. 1998; Alves et al. 2007; Könyves et al. 2010). This resemblance between the CMF and IMF appears to suggest that the identified cores are the immediate precursors of stars. One fundamental difference, however, between the CMF and the IMF is the turnover mass, i.e., the peak at the low-mass part. Observed CMFs usually have larger turnover masses than observed IMFs (Alves et al. 2007; Nutter & Ward-Thompson 2007; Könyves et al. 2010). The previous studies proposed that this difference is consistent with the idea that about half of each core mass is blown out by stellar feedback such as protostellar outflows and stellar winds (Matzner & McKee 2000; Alves et al. 2007). However, recent observations of CMF in the W43-MM1 high-mass star-forming region revealed a CMF with a shallower slope. This might indicate that the CMFs evolve with time (Motte et al. 2018). On the other hand, Bontemps et al. (2001) revealed that the CMF in ρ Oph has a turnover mass similar to that of the mass function of Class II objects in this region. This indicates that almost all the core masses should go into the stars formed. Ikeda, Sunada, and Kitamura (2007) discussed the effect of confusion among cores on the CMF in Orion A, especially to the low-mass part. They claimed that there is no turnover in the confusion-corrected CMF and the observed turnover is not made by any physical processes.

Most of the previous studies on CMFs have used the dust continuum emission (Motte et al. 1998, 2018; Alves et al. 2007; Nutter & Ward-Thompson 2007; Könyves et al. 2010; Liu et al. 2018; Kong 2019; Sanhueza et al. 2019). In general, the dust emission is optically thin on the cloud scale and thus it is an excellent tracer of the cloud column density since the spatial variation of the dust-to-gas mass ratio is believed to be small. However, the core is a dense structure embedded in the parent cloud. Thus, it seems to be very difficult to estimate the core masses from the 2D dust emission maps accurately. In other words, it is crucial to estimate the core masses by removing the ambient gas outside the core. In this paper, we call gas components that are not associated with the core along the line of sight "ambient gas." In this sense, the previous studies of the CMFs based on the dust emission and extinction maps tend to overestimate the core masses.

In this paper, toward a full understanding of the relationship between the CMF and IMF, we attempt to identify the cores in the Orion A Giant Molecular Cloud using 3D position–position–velocity data of wide-field $C^{18}O$ mapping and estimate the core masses using the Herschel–Planck column density map (Lombardi et al. 2014) by removing the contribution of the ambient gas. It is worth noting that previous studies have demonstrated that real structures in molecular clouds are reasonably related to the structures identified in the position–position–velocity data (Williams et al. 1994; Rosolowsky et al. 2008; Goodman et al. 2009).

Orion A is the most studied giant molecular cloud (Bally et al. 1987; Genzel & Stutzki 1989; Hillenbrand 1997; Ikeda et al. 2007; Shimajiri et al. 2011; Nakamura et al. 2012; Tatematsu et al. 2016; Hacar et al. 2017). The distance to the cloud is derived to be 414 pc based on the very-long-baseline interferometry observations (Menten et al. 2007). Thus, it is one of the nearest giant molecular clouds. Orion A also contains the nearest ongoing high-mass star formation site in the Orion Nebula cluster. Near-infrared observations also indicate that younger populations are more abundant, i.e., star formation is accelerated (Palla & Stahler 1999). Recently, we have obtained wide-field maps of this region in ^{12}CO ($J = 1$–0), ^{13}CO ($J = 1$–0), and $C^{18}O$ ($J = 1$–0) with the Nobeyama 45 m telescope (Feddersen et al. 2018; Nakamura et al. 2019; Ishii et al. 2019; Tanabe et al. 2019). Among the three CO isotopologues, the $C^{18}O$ emission is expected to trace denser structures with densities of $\sim 10^4 \, cm^{-3}$. Recent studies by Pety et al. (2017) and Gratier et al. (2021) also demonstrated that the $C^{18}O$ emission reasonably traces the high-column density molecular gas with $N_{H_2} \sim 10^{22} \, cm^{-3}$. The wide-field H_2 column density map obtained from the Herschel observations, which is derived from the dust emission, is also available (Lombardi et al. 2014). Thus, Orion A is one of the suitable star-forming clouds to assess the contribution of the ambient gas mass to the core mass estimate.

This paper is organized as follows. In section 2, we present the details of the observations and data. In section 3, we describe the global distribution of the dense molecular gas with the $C^{18}O$ data. Then, we show the results of the core identification in section 4. Here, we adopt Dendrogram and define a leaf as a core, following the previous studies In section 5 we present the CMF derived from the $C^{18}O$ data. We also compare our results with previous studies of the CMF in Orion A. In section 6 we compare the CMF derived from the $C^{18}O$ data and dust continuum
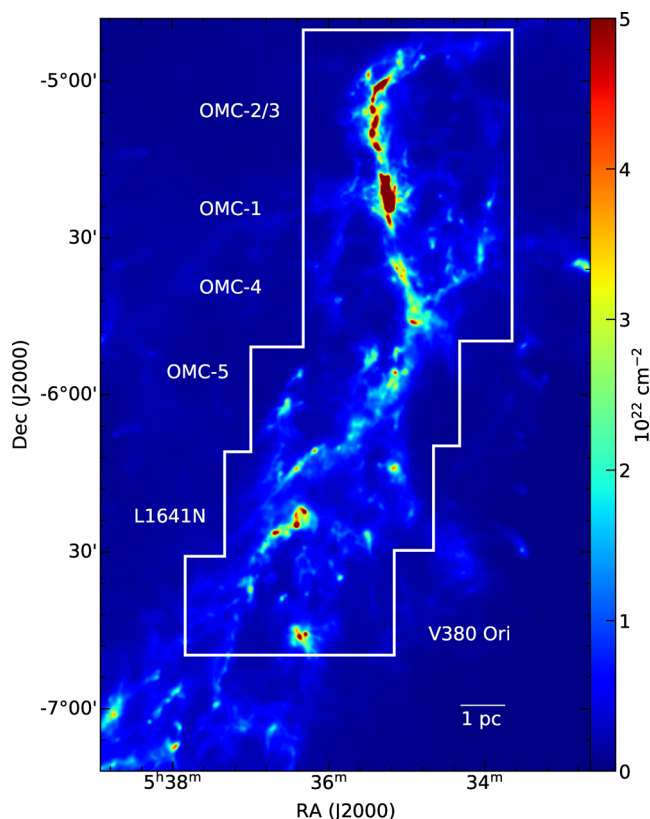
Fig. 1. $C^{18}O$ ($J = 1$–0) observation area overlaid on the Herschel–Planck H_2 map (Lombardi et al. 2014). The observed area is indicated with the white solid line. Our map covers a wide area of $1° \times 2°$ which is from OMC-1/2/3/4 to L 1641 N, and V380 Ori. (Color online)

emission (Nutter & Ward-Thompson 2007). Finally, we briefly summarize our results in section 7.

2 Observations and data

2.1 $C^{18}O$ ($J = 1$–0)

We carried out on-the-fly (OTF) mapping observations of $C^{18}O$ ($J = 1$–0, 109.782182 GHz) toward Orion A using the FOREST (Minamidani et al. 2016) receivers mounted on the NRO 45 m telescope. Our map covers a $1° \times 2°$ area which contains OMC-1/2/3/4, L 1641 N, and V380 Ori. Figure 1 shows the observed area of the $C^{18}O$ emission overlaid on the H_2 column density map obtained with the procedure described in the next subsection.

The details of the FOREST observations are described in Nakamura et al. (2019). In brief, the observations were done in the period from 2016 March to 2017 March. The telescope beam size (half-power beamwidth) is $\sim 15''$ at 110 GHz and the typical pointing accuracy was $3''$. The effective angular resolution of the data product is $\sim 21''$ (full width at half maximum; FWHM) after convolving by a spheroidal function with a spatial grid size of $7''.5$. In this paper, the data was additionally smoothed to reduce the

noise level of the map. The $C^{18}O$ map has an effective resolution of $\sim 26''.4$ (FWHM), corresponding to ~ 0.05 pc at a distance of 414 pc, and a velocity resolution of ~ 0.1 km s^{-1}. The typical rms noise level of the C18O data is $1\sigma = 0.33$ K in terms of T_{MB}. It is worth noting that the original map provides a higher angular resolution of $\sim 21''$, but we smoothed the data to a lower angular resolution to reduce the noise level. We used the data taken only with the FOREST receiver in this paper. Ikeda and Kitamura (2009) derived the CMF in a square degree area of Orion A from $C^{18}O$ ($J = 1$–0) observations with the comparable resolution taken by the same telescope. We compare the result of our analysis with Ikeda and Kitamura (2009) in subsection 5.3. Our observations cover a larger area of $1° \times 2°$ than that of Ikeda and Kitamura (2009), who conducted the mapping observations toward the Orion Nebula Cluster region in a full-beam sampling mode with a previous receiver, BEARS, and the noise level of our map (0.33 K) is better than theirs (0.45 K). The velocity resolution of ~ 0.1 km s^{-1} is almost similar to each other. The integrated intensity map of the $C^{18}O$ ($J = 1$–0) emission is shown in figure 2a.

2.2 H_2 column density data

We also used the Herschel–Planck H_2 column density map (Lombardi et al. 2014; Stutz & Kainulainen 2015) to calculate the core masses. The original Herschel data have an effective angular resolutions of $18''$ and $36''$ at 250 and $500 \mu m$, respectively. The temperature map with $36''$ and $250 \mu m$ continuum emission map with $18''$ are used to make the column density map. See Stutz and Kainulainen (2015) for the actual procedure. Then, we smoothed the $18''$ data to match the $C^{18}O$ effective angular resolution of $26''.4$, with a grid of $7''.5$.

2.3 Catalog of young stellar objects (YSOs)

In order to distinguish starless cores from protostellar cores, we used a catalog of YSOs from the Herschel Orion Protostar Survey (HOPS) (Furlan et al. 2016). This catalog contains 36 Class 0 sources and 38 Class I sources in our observed area. In this paper, we use the 74 Class 0 and Class I sources as HOPS YSOs.

3 Global distribution of the $C^{18}O$ emission

Figures 2b and 2c show the maps of the intensity weighted velocity and the velocity dispersion of Orion A. The $C^{18}O$ emission follows the long filamentary structure, which includes the OMC-1/2/3/4 regions and is called the Intengral-shaped Filament (ISF), well. Also, there is a velocity gradient along the ISF. The northern region has
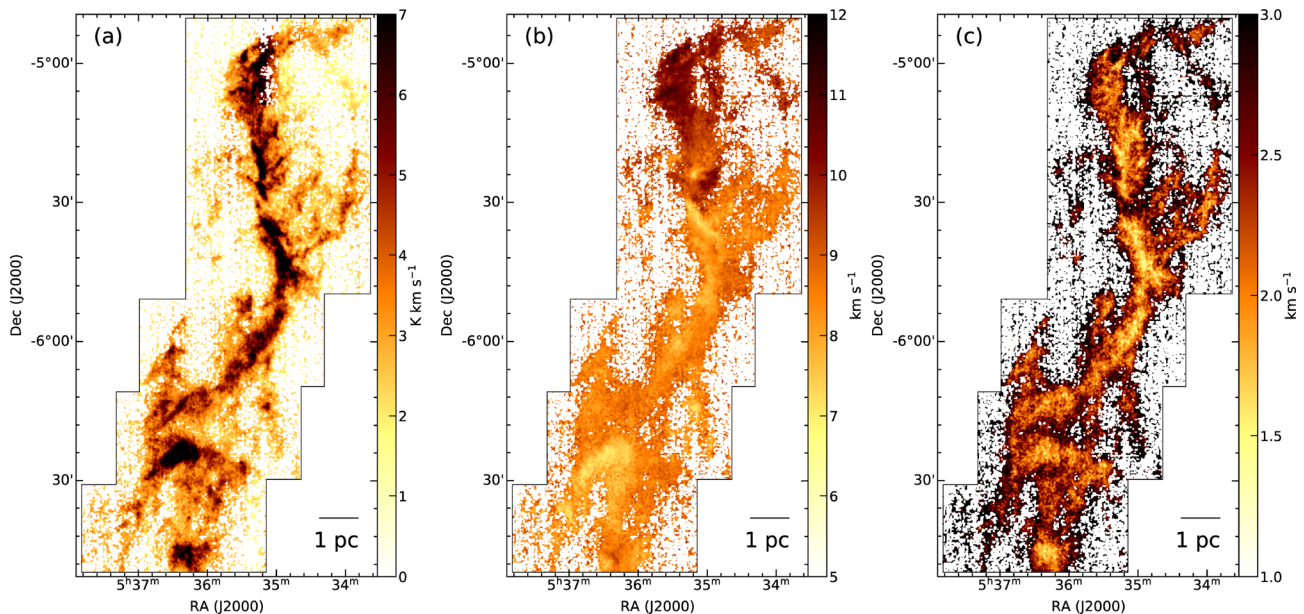
**Fig. 2.** (a) Integrated intensity map (moment-0 map) of the $C^{18}O$ ($J = 1$–0) emission, (b) intensity weighted coordinate (moment-1 map) and (c) intensity weighted dispersion of the coordinate (moment-2 map), respectively. The integration was done in the velocity range from ~ 3 to ~ 15 km s^{-1} for the pixels whose integrated intensity is larger than 15 local rms noise. We made these maps with the CASA software. The observed area is indicated with the black solid line in each panel. (Color online)

a velocity of ~ 12 km s^{-1} and the southern region such as L 1641 N has a velocity of ~ 5 km s^{-1}. The moment-1 map (figure 2b) also shows a sudden jump in the velocity from ~ 9 to ~ 5 km s^{-1} around the L 1641 N region, and the V380 Ori region has a velocity of ~ 9 km s^{-1}. In other words, two components with different velocities appear to overlap along the line of sight. Nakamura et al. (2012) suggested that these components may be colliding (see also Lim et al. 2021). In fact, some faint extended emission with intermediate velocities appears to connect with the two components in the position–velocity diagrams (see figure 8 in Nakamura et al. 2012). The OMC-1 region has a very complicated velocity structure, which presumably is affected by stellar feedback or global gravitational contraction along the ISF (Hacar et al. 2017; Ishii et al. 2019) and cloud–cloud collision (Fukui et al. 2018). The moment-2 map (figure 2c) indicates that the velocity dispersion tends to be larger toward brighter regions inside the ISF.

Figure 3 shows the optical depth of $C^{18}O$ in Orion A. Here, we adopted equation (6) in Nakamura et al. (2019) with the excitation temperature derived with their equation (3). The maximum optical depth is about 0.2 and thus we assume that the $C^{18}O$ emission is optically thin in the entire area.

4 Core identification

There are at least two main approaches to identify the dense cores in molecular clouds. One is to use dust emission or
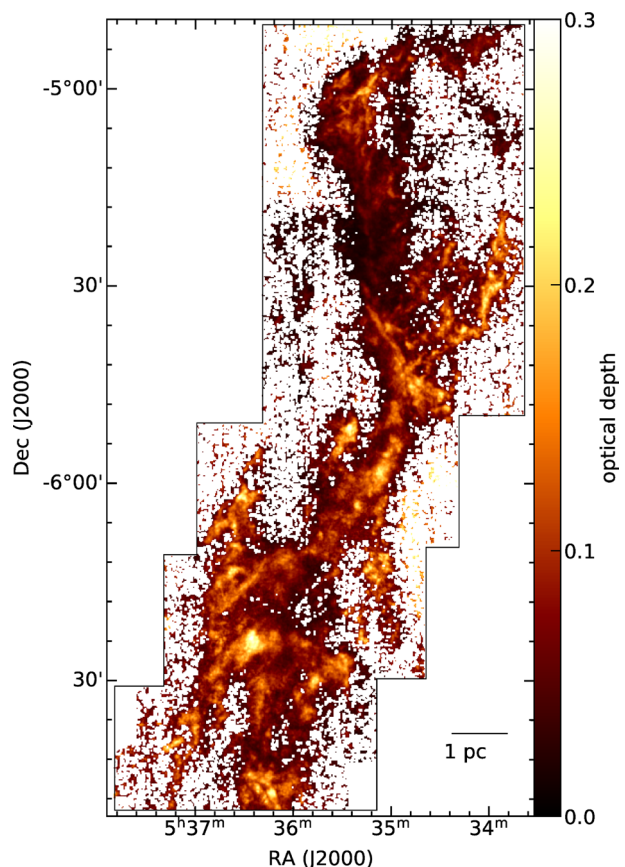
Fig. 3. Optical depth of the $C^{18}O$ ($J = 1$–0) emission in Orion A. We calculated the optical depth for the same pixels of figure 2 by using the temperature derived from ^{12}CO ($J = 1$–0) observations. (Color online)

extinction maps (e.g., Motte et al. 1998; Alves et al. 2007; Nutter & Ward-Thompson 2007; Cheng et al. 2018; Sanhueza et al. 2019). The other is to use molecular emission line data (e.g., Ikeda et al. 2007; Ikeda & Kitamura 2009; Maruta et al. 2010). The dust emission is considered to be an excellent tracer of the column density of molecular clouds or interstellar medium (ISM). However, the dust cores, which have a three-dimensional structure in nature, are identified on the basis of the two-dimensional position–position maps. It is difficult to distinguish the structures overlapped along the line of sight. The structure identification using molecular line emission allows one to distinguish overlapping structures along the line of sight by taking advantage of the three-dimensional position–position–velocity (p–p–v) data. This method assumes that the coherent structures in p–p–v space are closely related to actual structures in position–position–position (p–p–p) space. However, the fractional abundances of the interstellar molecules relative to the hydrogen gas often vary even in single clouds (Savva et al. 2003). Thus, the mass estimation would be significantly influenced by the spatial variation of the fractional abundances. In this sense, using these two tracers is complimentary for the structure identification in molecular clouds.

In this paper, we use the advantages of the two tracers for core identification. We first identify the dense cores using our $C^{18}O$ ($J = 1$–0) data cube with a velocity resolution of $0.1 \, \mathrm{km \, s^{-1}}$. Then, we use the Herschel–Planck H_2 column density map to estimate the masses of the cores identified from the $C^{18}O$ ($J = 1$–0) data. To evaluate the masses of the cores, we attempt to remove the contribution of the ambient gas to the core mass estimation using the $C^{18}O$ ($J = 1$–0) data. As shown above, the $C^{18}O$ emission is optically thin. However, the $C^{18}O$ molecule tends to be sometimes depleted in cold dense regions with $T \lesssim 20 \, \mathrm{K}$ (Caselli et al. 1999). In the presence of strong far UV radiation, selective dissociation changes the fractional abundances of CO and its isotopologue (Lada et al. 1994; Shimajiri et al. 2014; Lin et al. 2016; Ishii et al. 2019). These effects tend to destroy the linear relationship between the intensities of the dust emission and the optically thin $C^{18}O$ emission.

4.1 Dendrogram and dense cores

We applied astrodendro ver. 0.2.0 to the three-dimensional (p–p–v) $C^{18}O$ data.[1] The algorithm searches the hierarchical structures in the 2D data (position–position) or 3D data for given parameters. Astrodendro has three input parameters, (1) `min_value`, (2) `min_delta`, and (3) `min_npix`. It keeps searching the local peaks from the highest value of the data

to the lowest value specified by `min_value` in the interval of `min_delta`. The local peak is called `leaf` in the algorithm. In addition, the number of pixels contained in a leaf should be greater than `min_npix`.

Two leaves are merged into one structure called `branch` when the bottoms of both leaves are larger than `min_value`. After that, two branches are merged into a new branch or a `trunk` which is the lowest structure. Then, the result of the identification is depicted with a tree-like diagram. A more detailed description and discussion about the algorithm are given in Rosolowsky et al. (2008). (See also Goodman et al. (2009) for the application to the 3D molecular line data.) In this study, we adopted `min_delta` $= 2\sigma$, `min_value` $= 2\sigma$, and `min_npix` $= 30$ which corresponds to the volume of one beam times three channels for our structure identification. We define a leaf as a dense core of the molecular cloud. We note that this core definition is reasonably verified by the synthetic observations of the turbulent cloud simulations (Burkhart et al. 2013; Beaumont et al. 2013), although the structures identified in the real p–p–p space do not perfectly match with those identified in the p–p–v space. In addition, the structure identification in the p–p–v space also depends on cloud environments.

Since the observations were carried out in various atmospheric conditions for a couple of years, the rms noise level of the map is not uniform over the observed area. The value of `min_value` does not always correspond to twice the noise level. To minimize the effect of the non-uniform noise levels in the core identification, we imposed the following three conditions for identified leaves with the parameters mentioned above. Condition (1): The peak intensity of the identified leaf should be four times larger than the local rms noise level at the corresponding spatial position. Condition (2): More than three successive channels ($\sim 0.3 \, \mathrm{km \, s^{-1}}$) should contain more than nine pixels for each channel. This threshold pixel number of nine is equivalent to one effective angular resolution of the map ($\approx 26{.}''4$). Condition (3): An identified core should not contain any pixels located at the boundaries of the observation area. In total, we identified 746 cores.

Then, we classified the identified cores into two groups using the HOPS catalog, starless and protostellar cores. If an identified core overlaps spatially with at least one HOPS object on the plane of the sky, we classified it as a protostellar core. Here we classified an identified core as a protostellar core when it contains more than one HOPS object within the area projected on to the plane of the sky. A core without any overlapped HOPS objects is categorized as a starless core.

As a result, we identified 709 starless cores and 37 protostellar cores (table 1). Figure 4 shows the result of the core identification. The starless cores and the protostellar

---

[1] ⟨https://dendrograms.readthedocs.io/en/stable/⟩.

Table 1. Results of core identification in Orion A.

Category	N
Identified core	746
Starless core	709
Protostellar core	37
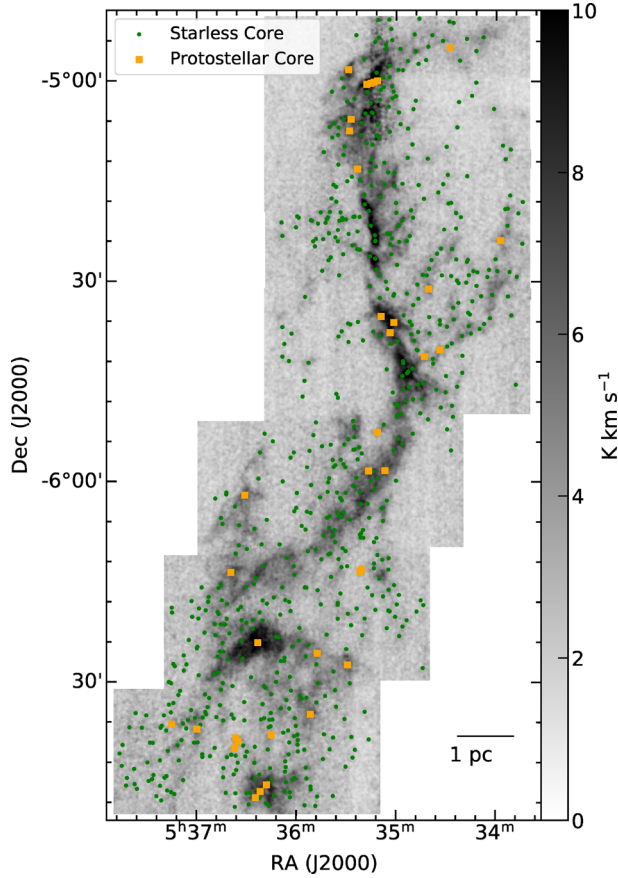
Fig. 4. Identified starless cores (green circles) and protostellar cores (orange squares) are plotted on the integrated intensity map of the C^{18}O emission. (Color online)

cores are plotted on to the integrated intensity map of the C^{18}O emission and most cores are distributed along the ISF. Among the 74 HOPS Class 0/I objects, 34 ($\sim$46%) objects were not identified as our protostellar cores. However, most of the HOPS Class 0/I objects are associated with local C^{18}O peaks and they are excluded from our samples by the additional thresholds of core identification. To identify these protostellar cores, we need data with better sensitivities.

4.2 Derivation of the core physical quantities

4.2.1 Core radius, aspect ratio, and velocity dispersion
We define the physical quantities of the identified cores as follows. The positions and the line-of-sight velocity of a core are determined by the mean positions of the structure

identified and the intensity-weighted first-moment velocity, respectively. The core radius is defined as

$$R_{\text{core}} = \left(\frac{A}{\pi}\right)^{1/2} , \qquad (1)$$

where A is the exact area of the core projected on to the plane of the sky. The aspect ratio of the core is calculated as the ratio of the major and minor axes. The major and minor axes in half width at half maximum (HWHM) are computed from the intensity-weighted second moment in the direction of greatest elongation and perpendicular to the major axis, respectively, in the plane of the sky. The position angle of the core is determined counter-clockwise from the +RA axis. The velocity width in FWHM, dV_{core}, is obtained by multiplying the intensity-weighted second moment of velocity by a factor of $2\sqrt{2\ln2}$. Figures 5a, 5b, and 5c show the histograms of the diameter, aspect ratio, and velocity width in FWHM. The minimum, maximum and mean value with standard deviation of each physical property of the identified cores are summarized in table 2. The mean values and standard deviation of diameter, aspect ratio, and velocity width in FWHM of identified cores are 0.16 ± 0.06 pc, 0.58 ± 0.16, and 0.33 ± 0.14 km s^{-1}, respectively. Starless cores tend to have a small diameter and velocity width compared to protostellar cores. There are no clear differences between the aspect ratios of starless cores and protostellar cores.

4.2.2 Core mass and virial mass
To estimate the core mass with minimizing the effect of the CO depletion, we used the Herschel–Planck H$_2$ column density data in a different way from previous studies on the core identification based on C^{18}O observations (Ikeda et al. 2007; Ikeda & Kitamura 2009; Shimajiri et al. 2015). We determined the core mass by integrating the Herschel–Planck H$_2$ mass over the projected area of the core on the plane of the sky defined by Dendrogram on the C^{18}O image. The dendrogram analysis allows us to distinguish between the cores and other structures. In other words, we can estimate the contribution of the emission associated with cores on the integrated intensity [see also the left-hand panel of figure 4 and sub-subsection 4.1.2 in Rosolowsky et al. (2008)]. When multiple pixels belonging to the different cores are overlapped along the line of sight at a pixel, we divide the Herschel–Planck H$_2$ mass between cores in proportion to the integrated intensity of C^{18}O emission after removing the contribution of the ambient gas. Thus, the mass of the kth core is calculated as

$$M_{\text{core}}^k = \mu m_{\text{H}} \times \sum_i \left(N_{\text{H}_2,i} \times F_i^k\right) \qquad (2)$$
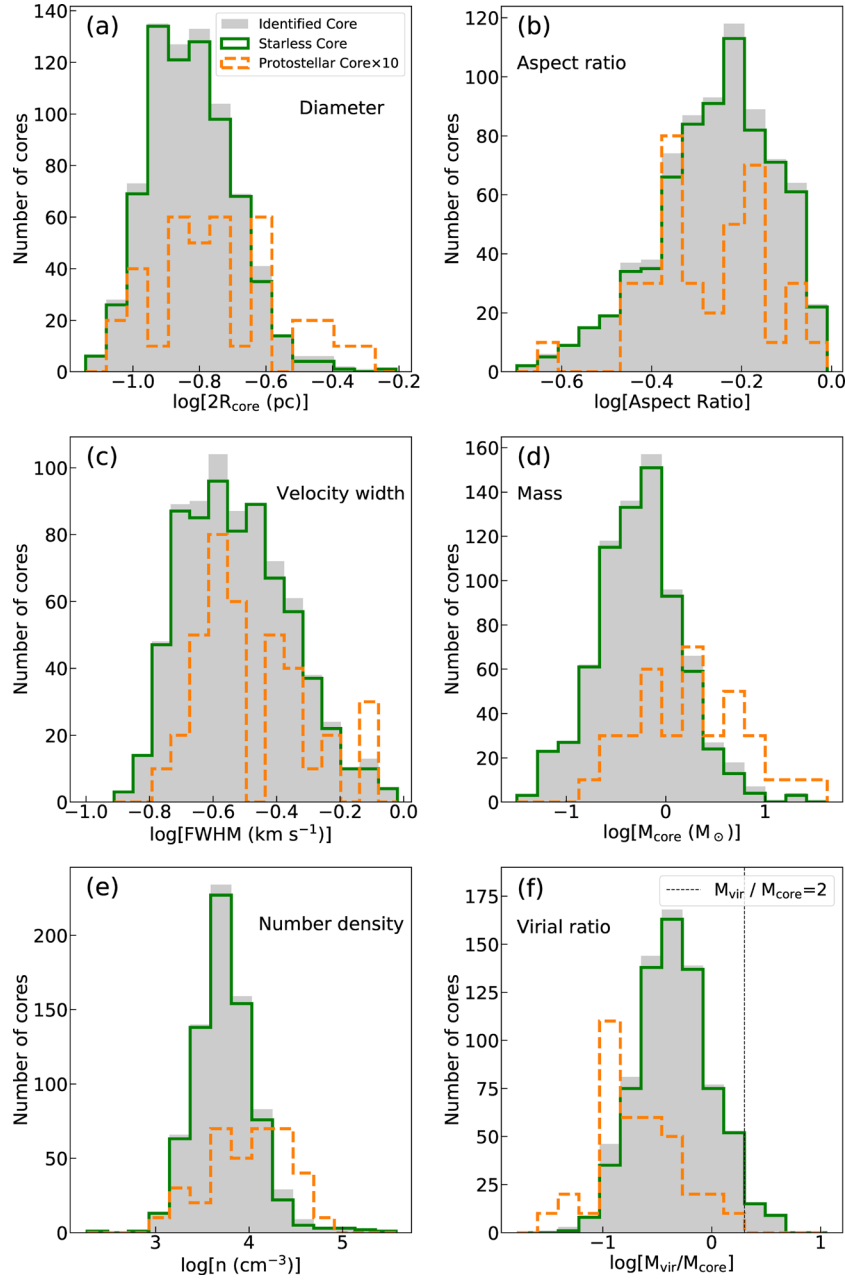
Fig. 5. Histograms of (a) the diameter (b) the aspect ratio, (c) the FWHM velocity width, (d) the core mass, (e) the number density, and (f) the virial ratio of $C^{18}O$ cores calculated from $C^{18}O$ observation, respectively. The histogram for all identified cores is shown in grey. The green and orange histograms are for starless cores and protostellar cores. The vertical line in panel (f) shows $M_{core}/M_{vir} = 2$. (Color online)

where $F_i^k = I_i^k/T_i$ is the intensity fraction at the ith pixel for the kth core to the sum of emission of all trunks, I_i^k is the $C^{18}O$ integrated intensity at the ith pixel for the kth core, and $T_i (= \int_{trunk} I_i dv)$ is the total velocity-integrated intensity at the ith pixel in all trunks, $\mu = 2.3$ is the mean molecular weight, m_H is the mass of a hydrogen atom, and $N_{H_2, i}$ is the Herschel–Planck H_2 mass contained in the ith pixel. We discuss the influence of the warm ambient gas (trunk) on this method in appendix 1. About 60% of identified cores overlap with more than one core (see appendix 2

for details). Here we classified a pair of identified cores as overlapped cores when they overlapped more than one pixel along the line of sight. The above expression can be rewritten as

$$M_{core}^k = 4.15 \times 10^{-2} \left(\frac{\theta}{7\rlap{.}''5} \right)^2 \left(\frac{D}{414 \text{ pc}} \right)^2$$
$$\times \left(\frac{\sum_i N_{H_2, i, k} F_i^k}{10^{22} \text{ cm}^{-2}} \right) M_\odot \quad (3)$$

Table 2. Summary of core properties in Orion A.

Property	Category	Minimum	Maximum	Mean ± std.
Diameter (pc)	Identified core	0.07	0.62	0.16 ± 0.06
	Starless core	0.07	0.62	0.16 ± 0.05
	Protostellar core	0.08	0.50	0.20 ± 0.10
Aspect ratio	Identified core	0.20	0.98	0.58 ± 0.16
	Starless core	0.20	0.98	0.58 ± 0.16
	Protostellar core	0.24	0.92	0.56 ± 0.16
FWHM (km s^{-1})	Identified core	0.12	0.96	0.33 ± 0.14
	Starless core	0.12	0.96	0.32 ± 0.14
	Protostellar core	0.18	0.81	0.36 ± 0.16
Mass ($M_\odot$)	Identified core	0.03	42.00	1.08 ± 2.42
	Starless core	0.03	24.45	0.92 ± 1.65
	Protostellar core	0.18	42.00	4.12 ± 7.51
Number density (10^4 cm^{-3})	Identified core	0.02	37.36	0.87 ± 1.92
	Starless core	0.02	37.36	0.84 ± 1.94
	Protostellar core	0.12	6.53	1.54 ± 1.38
Virial ratio	Identified core	0.03	19.45	0.64 ± 0.89
	Starless core	0.05	19.45	0.66 ± 0.91
	Protostellar core	0.03	1.46	0.31 ± 0.30

The virial mass of a core is estimated as

$$M_{\rm vir} = 210 \left(\frac{R_{\rm core}}{\rm pc} \right) \left(\frac{dV_{\rm core}}{\rm km\,s^{-1}} \right)^2 M_\odot \qquad (4)$$

where $dV_{\rm core}$ is the FWHM velocity width, the core is assumed to be an uniform sphere, and magnetic fields and external pressures are neglected for dynamical support. The virial ratio is defined as

$$\alpha_{\rm vir} = \frac{M_{\rm vir}}{M_{\rm core}} \, . \qquad (5)$$

We note that for a centrally-condensed sphere with $\rho \propto r^{-2}$ the virial ratio becomes smaller by a factor of 5/3 than the above definition. The cloud shape also influences the actual value of the virial parameter (Bertoldi & McKee 1992). If the CO depletion is significant particularly in cold dense regions, the estimates of the line-widths in the cold starless cores may be somewhat affected.

In this paper, we define a core with a virial ratio smaller than 2 as a gravitationally bounded core. Then, we identified 684 bound starless cores and 25 unbound starless cores. All protostellar cores are likely to be bounded by gravity. Figure 6, the virial ratio–mass relation, shows the clear trend that more massive cores tend to have smaller virial ratios. The minimum, maximum, and mean value with standard deviation of each physical property of the identified cores derived in this section are also summarised in table 2. The mean values with standard deviation of the mass, number density and virial ratio of identified cores are $1.08 \pm 2.42\,M_\odot$, $(0.87 \pm 1.92) \times 10^4$ cm^{-3} and 0.64 ± 0.89, respectively.
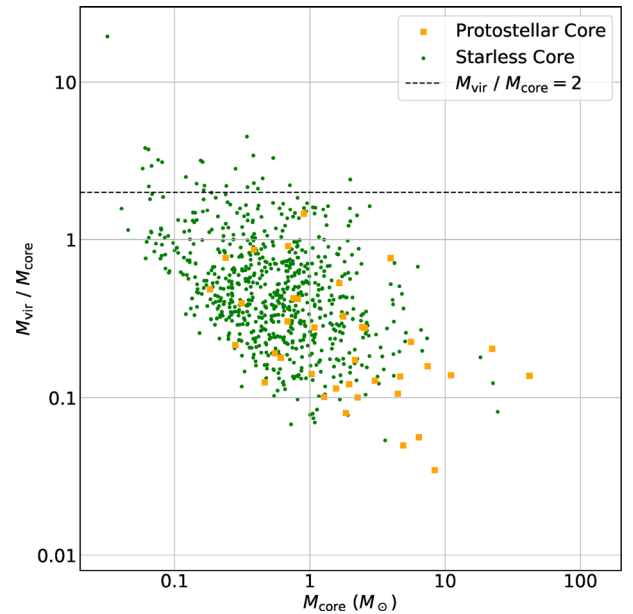
Fig. 6. Virial ratio ($M_{\rm core}/M_{\rm vir}$)–core mass relation. The horizontal dashed line shows $M_{\rm core}/M_{\rm vir} = 2$. The starless cores and protostellar cores are shown as green dots and orange squares, respectively. (Color online)

We assumed the local thermodynamic equilibrium (LTE) condition and optically thin emission of the C^{18}O ($J = 1$–0) to derive the mean column densities of the C^{18}O of individual cores. Here, we assigned the individual excitation temperature derived from ^{12}CO observation (see Nakamura et al. 2019) to each core. The mean excitation temperature of projected areas of cores is 33 K. We then calculated the fractional abundance of C^{18}O, $X_{\rm C^{18}O}$, for each core as a ratio of the column density of the C^{18}O and H$_2$. The mean

Table 3. Properties of identified cores (1).*

ID	RA[†] (h m s)	Dec[†] (° ′ ″)	v_{LSR} (km s^{-1})	A (arcsec^2)	$2R_{core}$ (″)	$2R_{core}$ (pc)	a_{major} (″)	a_{minor} (″)	PA (°)	dV_{core} (km s^{-1})	YSO
1	5 33 44.7	−5 18 5	9.3	5738	85	0.17	21.8	19.3	−149	0.38	N
2	5 33 45.0	−5 24 24	8.2	2756	59	0.12	25.0	10.8	89	0.18	N
3	5 33 47.3	−5 19 48	8.3	2925	61	0.12	30.8	8.9	84	0.17	N
4	5 33 48.2	−5 29 20	7.9	5119	81	0.16	34.1	9.1	61	0.28	N
5	5 33 48.7	−5 45 29	7.7	2925	61	0.12	20.5	13.6	74	0.22	N
6	5 33 51.5	−5 35 7	8.0	8100	102	0.20	24.3	20.3	−175	0.34	N
7	5 33 51.9	−5 10 15	10.5	2756	59	0.12	16.2	11.1	80	0.25	N
8	5 33 52.2	−5 17 8	10.2	3263	64	0.13	24.3	12.5	−138	0.19	N
9	5 33 52.6	−5 28 36	8.4	2475	56	0.11	27.9	8.9	59	0.25	N
10	5 33 53.4	−5 32 17	8.1	5794	86	0.17	23.7	15.1	145	0.34	N

*A complete listing of this table is available in the supplementary data section of the online version.
[†]Coordinates in J2000.0.

Table 4. Properties of Identified Cores (2).*

ID	T_{mb}^{peak} (K)	T_{mb}^{total} (K)	M_{core} ($M_{\odot}$)	M_{vir}/M_{core}	$\overline{n}$ (10^4 cm^{-3})	$\overline{T}_{ex}$ (K)	$\overline{N}_{C^{18}O}$ (10^{15} cm^{-2})	$\overline{X}_{C^{18}O}$ (10^{-7})
1	1.7	183.0	0.7	0.7	0.5	20.3	0.5	2.8
2	2.9	154.2	0.2	0.5	0.3	21.9	1.5	7.5
3	1.5	84.4	0.2	0.3	0.4	21.9	1.0	4.9
4	3.5	522.1	0.6	0.4	0.5	23.5	2.7	7.1
5	1.4	66.9	0.3	0.4	0.5	14.1	0.9	7.8
6	2.9	687.8	1.7	0.3	0.7	23.6	1.5	3.6
7	1.9	115.6	0.3	0.5	0.5	25.2	1.4	3.6
8	1.6	89.0	0.6	0.1	0.9	28.8	1.3	5.2
9	3.3	236.4	0.2	0.6	0.6	23.6	2.7	6.7
10	2.8	460.8	0.8	0.5	0.5	23.7	1.9	3.8

*A complete listing of this table is available in the supplementary data section of the online version.

value is $\overline{X_{C^{18}O}} = 5.7 \times 10^{-7}$, which is three times larger than the representative value of 1.7×10^{-7} (Frerking et al. 1982). Also, the number density of a core is obtained by assuming that the core has a constant density with a radius R_{core}. The physical properties of the identified starless and protostellar cores such as core mass, virial ratio, density, and C^{18}O fractional abundance are summarized in tables 3 and 4, respectively.

Figures 5d, 5e, and 5f show the histograms of mass, virial ratio, and number density of the C^{18}O cores. It is clear that protostellar cores are more massive and denser than starless cores. A large fraction of identified cores have a virial ratio of less than 2 and protostellar cores tend to have smaller virial ratios.

5 Discussion

5.1 Comparison between the C^{18}O emission and dust emission

Figure 7 shows the relationship between the H$_2$ column density derived directly from the C^{18}O integrated intensity, $N_{H_2,C^{18}O}$, and the Herschel–Planck H$_2$ column density, $N_{H_2,Herschel}$, in Orion A. The relationship is shown as a 2D histogram of PDF (probability distribution function) in panel (a) and contour in panel (b). Here, we obtained the C^{18}O column density under the assumption of LTE and optically thin condition as Ikeda and Kitamura (2009) and Shimajiri et al. (2015). The excitation temperature of C^{18}O was assumed to be the same as the peak intensity of ^{12}CO emission. We have calculated the C^{18}O column density of pixels which integrated intensity of trunks is larger than 15 local rms noise. We then converted the C^{18}O column density to the H$_2$ column density with a constant fractional abundance of C^{18}O to H$_2$ of $X_{C^{18}O} = 5.7 \times 10^{-7}$. The plot indicates that the column density of C^{18}O is roughly proportional to the Herschel–Planck H$_2$ column density below $N_{H_2} \lesssim 5 \times 10^{22}$ cm^{-2}. In figure 7a, the two dashed lines show $N_{H_2,C^{18}O} = 0.5 N_{H_2,Herschel}$ and $N_{H_2,C^{18}O} = 2 N_{H_2,Herschel}$. For larger H$_2$ column densities ($n \gtrsim 10^5$ cm^{-3}), the C^{18}O column density tends to level off. The number of such pixels is only 18.2%. In figure 7b, the identified cores are plotted on the contour. For most of the cores identified, the C^{18}O
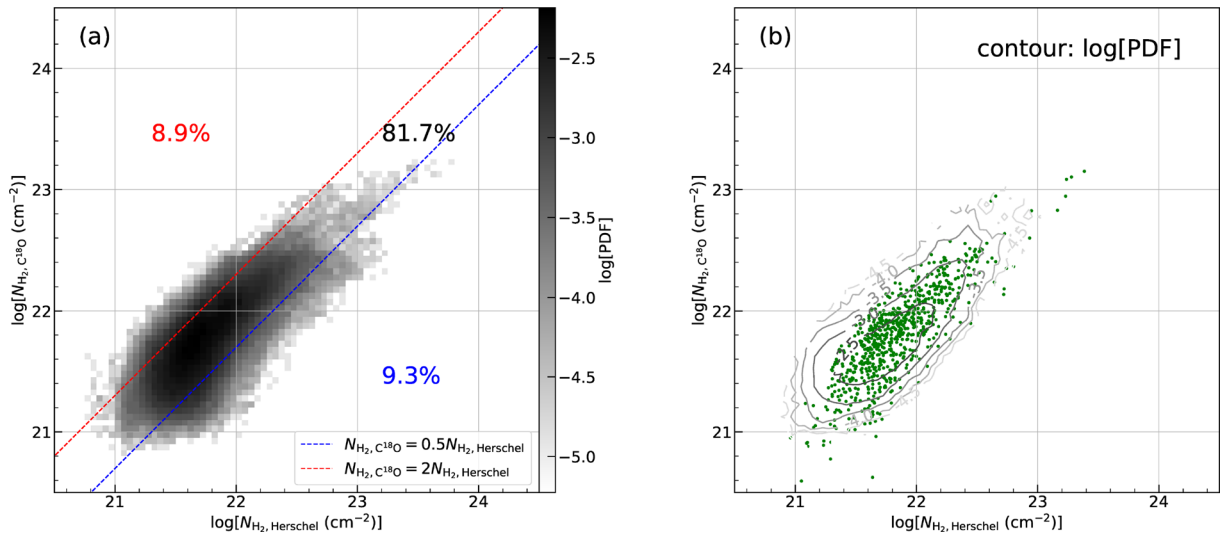
Fig. 7. Relationship between the H_2 column density derived directly from the $C^{18}O$ integrated intensity, $N_{H_2,C^{18}O}$, and the Herschel–Planck H_2 column density, $N_{H_2,Herschel}$ is shown as (a) a two-dimensional histogram of PDF and (b) contours. Here we calculated values of pixels whose integrated intensity is larger than 15 local rms noise in the projections of all identified trunks on to the sky plane. The blue and red dashed lines in panel (a) show $2N_{H_2,C^{18}O} = N_{H_2,Herschel}$ and $N_{H_2,C^{18}O} = 2N_{H_2,Herschel}$. $N_{H_2,C^{18}O}$ is the column density of H_2 calculated form the $C^{18}O$ $(J = 1–0)$ observations and mean abundance ratio of $C^{18}O$. $N_{H_2,Herschel}$ is the column density of H_2 derived from Herschel observations. Each percentage represents the fraction of N in each range: $N_{H_2,C^{18}O}/N_{H_2,Herschel} > 2$ (red), $1/2 \leq N_{H_2,C^{18}O}/N_{H_2,Herschel} \leq 2$ (black), and $N_{H_2,C^{18}O}/N_{H_2,Herschel} < 1/2$ (blue). In panel (b), the contour is drawn from $\log[PDF] = -4.5$ to -2.5 every $\log[PDF] = 0.5$. The dots show all identified $C^{18}O$ cores. The mean values of $N_{H_2,C^{18}O}$ and $N_{H_2,Herschel}$ in the projections of cores on to the plane of the sky are used to plot cores on to the figure. (Color online)

column density is more or less proportional to the Herschel–Planck H_2 column density. Thus, $C^{18}O$ is likely to be a reliable tracer of the molecular hydrogen mass with the exception of cold and dense regions with $N_{H_2} \gtrsim 5 \times 10^{22}$ cm^{-2}.

For dense regions, $C^{18}O$ appears to be less abundant. Therefore, the cores located in the dense regions may not be traced well by $C^{18}O$ emission. However, the number fraction of such cores is likely to be small for the entire Orion A. There may be at least two reasons why $C^{18}O$ abundance is lower toward denser regions. One is the CO depletion on to the grain surfaces for cold ($T \lesssim 20$ K), dense ($n \gtrsim 10^5$ cm^{-3}) parts. Another is the dissociation due to far-ultraviolet radiation (Shimajiri et al. 2014; Lin et al. 2016; Ishii et al. 2019). In Orion A, several massive stars, mainly located in the OMC-1 region, emit strong UV radiation, which can dissociate $C^{18}O$ in dense regions where ^{12}CO and ^{13}CO emissions become optically thick.

Our result is consistent with that of Ripple et al. (2013) with ^{13}CO. They showed that the effect of CO freeze-out is limited to regions with $N_{H_2} \gtrsim 10^{22}$ cm^{-2} ($A_v \gtrsim 10$ mag) and gas temperatures less than ∼20 K for Orion.

5.2 Consideration of the effect of the ambient gas to mass estimation

In this section, we compare the core masses calculated using two different approaches. One is the core mass weighted by

the $C^{18}O$ emission (M_{core}) defined by equation (2) in subsubsection 4.2.2. The other ($M_{projection}$) is derived by summing up all Herschel–Planck H_2 column densities included in the projected area of a core to the plane of the sky without removing the ambient components of the gas. This is essentially the same as the mass estimation based on some core identification schemes such as `clumpfind` (Williams et al. 1994) and Fellwaker (Berry 2015). When multiple cores overlap along the line-of-sight, we distribute the Herschel–Planck H_2 column density to each core. The assigned H_2 column density of each core is proportional to the $C^{18}O$ intensity of a core. The difference between M_{core} and $M_{projection}$ is the treatment of ambient gas of the dense core. $M_{projection}$ is a sum of M_{core} and mass of the ambient gas along the line of sight. We then calculated the mass ratio $M_{core}/M_{projection}$ and show the mass ratio—Herschel–Planck H_2 column density relation in figure 8. As shown in this figure, an identified core with a higher H_2 column density tends to have a smaller mass ratio. This suggests that such cores have more ambient gas and the core mass derived from dust observations tends to be more overestimated. A large fraction of the core has a mass ratio of less than 0.5, and the mean mass ratio and standard deviation are 0.35 ± 0.21. Then, more than 50% of the H_2 column density seems to come from the ambient gas in the dense regions with H_2 column density $\gtrsim 10^{22}$ cm^{-2}. In other words, the mass estimated only from the 2D dust emission map is about three times larger than the actual mass evaluated in 3D. This
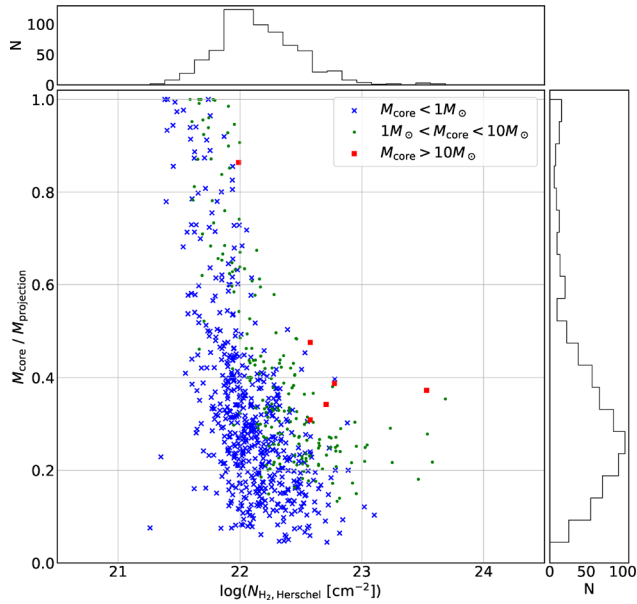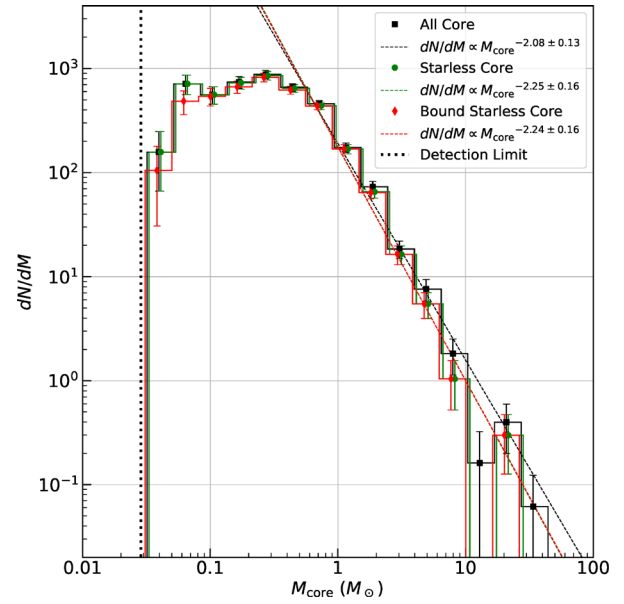
Fig. 8. Mass ratio $M_{core}\ M_{projection}-N_{H_2,Herschel}$ relation. To calculate $M_{projection}$, all H_2 column density is assigned to cores. When multiple cores overlap along the line of sight, H_2 column density proportional to each intensity is distributed to each core. The mean value and standard deviation of mass ratio $M_{core}/M_{projection}$ are 0.35 ± 0.21. The blue crosses, green circles, and red squares show the cores whose masses are $M_{core} < 1\,M_\odot$, $1\,M_\odot < M_{core} < 10\,M_\odot$, and $M_{core} > 10\,M_\odot$, respectively. (Color online)

Fig. 9. CMFs for the identified cores (black line), starless cores (green line), and gravitationally bound starless cores (red line). The error bars show the statistical uncertainty calculated as the square root of the number of cores in each mass bin, $\sqrt{N}$. The dashed line shows the best-fitting single power-law functions for each CMF between one mass bins above the turnover and the high-mass end. The dotted line shows the detection mass limit of $\sim 0.03\,M_\odot$. (Color online)

implies that the core masses estimated with the dust emission and extinction are significantly larger than the actual values. For further discussion, we need more observations with other molecular lines.

5.3 Core mass function in Orion A

In this section, we derive the CMF in Orion A using the cores identified above and M_{core} and then discuss their properties. Here, the CMF is defined as the number of cores with masses in a mass range from M_{core} to $M_{core} + dM_{core}$.

Figure 9 shows the CMFs for all identified cores, starless cores, and gravitationally bound cores. Since almost all identified cores seem to be bounded by gravity as shown in sub-subsection 4.2.2, we do not classify bound and unbound cores in order to derive CMFs in this paper. The mass detection limit for our analysis is $\sim 0.03\,M_\odot$. This mass is derived from the minimum intensity and size which pass the core identification conditions described in section 4 and assumptions of LTE condition and optically thin emission of $C^{18}O$ ($J = 1$–0) emission. Here we applied $T_{ex} = 33$ K and $X_{C^{18}O} = 5.7 \times 10^{-7}$. Both CMFs have turnovers at $\sim 0.3\,M_\odot$ and a power-law-like shape above the turnovers. The best-fitting power-law indexes of CMFs for all cores, starless cores, and gravitationally bound cores are -2.08, -2.25, and -2.24, respectively. The best-fitting power-law indices are in agreement with that of the

Salpeter IMF (-2.35, Salpeter 1955). The slopes in the CMFs are also consistent with the previous study (Ikeda & Kitamura 2009) that identified $C^{18}O$ cores using a different core identification scheme `clumpfind` in a much smaller area including the OMC-1 region ($\sim 2.4\,pc \times 2.4\,pc$). Their $C^{18}O$ data have the same effective angular resolution and velocity resolution as ours. However, the turnover mass of their CMF for the OMC-1 region, $\sim 5\,M_\odot$, is about three times larger than our value. This difference mainly comes from the usage of the different core identification schemes. For the Ikeda, Sunada, and Kitamura (2007) scheme, i.e., `clumpfind`, the core mass tends to be larger than that obtained based on Dendrogram since for the former all the pixels located inside the closed contour which contains cores are assigned to the adjacent core.

In order to estimate the completeness of core identification, we derived the detection probability as a function of the core mass by inserting the artificial cores to the observed cube data generated as follows.

1. We decided the mass of each artificial core as the central value of each mass bin on the log scale.
2. With the assumptions of the LTE condition and optically thin emission of the $C^{18}O$ ($J = 1$–0), we converted the mass of each artificial core to the integrated intensity of $C^{18}O$ emission using $T_{ex} = 33$ K and $X_{C^{18}O} = 5.7 \times 10^{-7}$.

3. We calculated the radius and velocity width of each core using the radius–mass and velocity width–mass relations, which are derived by fitting for all identified cores. Here we derived radius using the geometric mean of the major and minor axes of identified cores. The mean values of major and minor axes are shown in table 3.

4. We made a modified dataset by inserting the artificial cores that have the 3D Gaussian shape in the p–p–v space with sizes and velocity widths derived above. Here we just added the artificial cores to the observed data. The positions and the system velocities of the artificial cores that correspond with individual mass bins are given randomly in the trunks which are the lowest structures of Dendrogram's hierarchies.

5. We applied the same core identification method to the modified data and checked whether the artificial core is identified or not.

6. We repeated this procedure N_{trial} times for each mass bin in the CMF plot and calculated the possibility that the artificial cores are identified as independent cores $F(M_{LTE}/M_{\odot})$ with equation (6).

To calculate the probability that the artificial cores are identified as independent cores, first we prepared two sets of data; the original observed data and modified data which contains the artificial core. We applied the same core identification method described in section 4. Then, we counted the number of identified cores within 1σ from the center of the artificial core in observed data $n_{observed}$ and modified data $n_{artificial}$. We summed up the number of the cases of $n_{artificial} - n_{observed} \geq 1$ for $N_{trial} = 100$ trials as $n_{identified}$. Finally, the probability function that the artificial cores are identified as independent cores is derived as

$$P(M_{LTE}/M_{\odot}) = \frac{n_{identified}(M_{LTE}/M_{\odot})}{N_{trial}} \qquad (6)$$

Then, the corrected number of cores in each mass bin $N_{corrected}$ is calculated with the observed number of cores $N_{observed}$ as

$$N_{corrected} = \frac{N_{observed}}{P(M_{LTE}/M_{\odot})} \qquad (7)$$

Figure 10 shows the observed and compensated CMFs. The shape of the compensated CMF at the high-mass end is essentially the same as the observed one. In contrast, we see significant differences between the distribution at low-mass parts of observed CMF and compensated CMF. The number of low-mass cores in the observed CMF is smaller than that in compensated CMF and such cores are likely to be missed in the observed CMF. We find no clear turnover in the compensated CMF. Thus, it is difficult to conclude
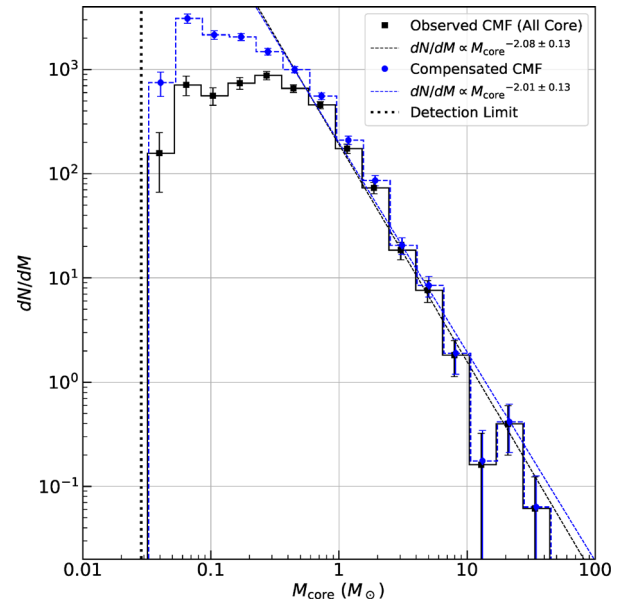

Fig. 10. Observed CMF (black line) and compensated CMF (blue line) for the identified cores. In compensated CMF, we derived the number of cores in each mass bin by dividing the observed number by detection probability. (Color online)

from our observations that the CMFs have a turnover at the low-mass part. This is consistent with the argument made by Ikeda, Sunada, and Kitamura (2007) This fact suggests that the spatial resolution of our data is not sufficient to confirm whether a CMF has a turnover, and thus we need a higher spatial resolution to address this point.

6 Comparison with the CMF derived from the dust emission

In subsection 5.2, we pointed out that the masses derived from the dust emission map tend to be significantly overestimated due to the contribution of the ambient gas. Here, we attempt to assess how this overestimation affects previous results by using Nutter and Ward-Thompson's (2007) core catalog. Figure 11 shows the CMF derived from the SCUBA 850 μm emission map with an angular resolution of $\sim$15″. The core identification scheme of Nutter and Ward-Thompson (2007) is also different from ours. They did not use a hierarchy but a signal-to-noise ratio; a detailed explanation can be found in their paper. The authors set the distance of Orion A as 400 pc and we recalculated the core masses with a distance of 414 pc. As a result, the turnover mass derived from the dust emission ($\sim$0.5 $M_{\odot}$) appears to be comparable to our value obtained from the $C^{18}O$ emission. However, the core mass estimated from continuum observation tends to be overestimated the core mass since the dust mass sums up both the core mass and the ambient gas overlapped along the line of sight. This is one of the
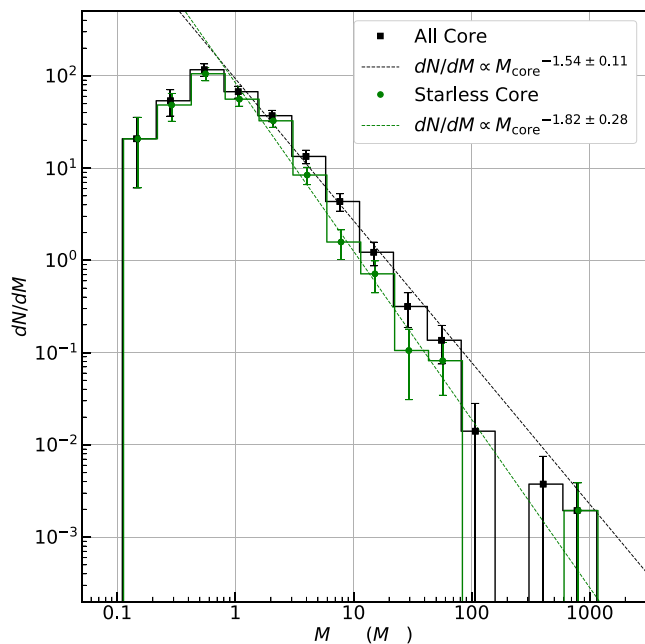
Fig. 11. CMFs of all dust cores and starless cores identified in Nutter and Ward-Thompson (2007) in Orion A. The dashed line shows the best-fitting single power-law functions for each CMF above the turnover as figure 9. (Color online)

disadvantages in estimating the core masses using only the dust observations. It is worth noting that in the SCUBA dust image the structures larger than $\sim1\rlap{.}'5$ are removed during the data reduction process. This artificial effect leads to underestimates of the dust emission.

In addition, the cores which overlap along the line of sight are difficult to distinguish using only the dust map. In fact, the most massive dust core in Nutter and Ward-Thompson (2007) has a mass of $\sim1062\,M_\odot$, located in OMC-1. In our $C^{18}O$ case, the most massive core has a mass of $\sim42\,M_\odot$. In the area containing the most massive dust core, our $C^{18}O$ data indicate the existence of multiple overlapping cores and/or a lot of ambient gas surrounding cores. This effect makes massive cores more massive and the slope of the CMF shallower toward the high-mass part, and this is another disadvantage for the dust observations. Figure 12 shows the histograms of physical properties of dust cores such as the core diameter, aspect ratio, mass, and density. Although the mass ranges of $C^{18}O$ cores and dust cores are similar, dust cores tend to be smaller than $C^{18}O$ cores. Thus, dust cores are likely to be denser than $C^{18}O$ cores. There are no big differences in aspect ratio between the two cores.

As derived in subsection 5.2, the dust mass may be overestimated by a factor of 3 from our data. If we apply this correction factor to Nutter's CMF, the turnover mass becomes small at 0.1–$0.2\,M_\odot$. This turnover mass is comparable to that of the stellar IMF in the Orion Nebular cluster (Hillenbrand 1997; Da Rio et al. 2012). If

we apply the same discussion as Alves (2007), this may indicate that the star formation efficiency (SFE) of individual cores is much higher than that predicted by the theoretical studies (Matzner & McKee 2000; Machida & Matsumoto 2012), in which SFE is estimated to be 30%–50% since the protostellar outflows blow out a significant amount of core mass. Such a high SFE appears to be consistent with the result of Bontemps et al. (2001). We note that recent numerical simulations have suggested that the mass infall from the surroundings plays an important role in the evolution of the core mass (Vázquez-Semadeni et al. 2019; Padoan et al. 2020). Such processes also affect the peak masses of CMFs, i.e., the turnover mass would evolve over time due to the mass accretion.

Considering the overestimation, the turnover mass is expected to be $\sim0.1\,M_\odot$, and observations with a higher angular resolution are needed to confirm it. In a forthcoming paper we will attempt to identify $C^{18}O$ cores in Orion A using the CARMA-NRO combined data (Kong et al. 2018) with a much higher angular resolution ($\sim8''$) to reveal the shape of the CMF at the low-mass part.

7 Summary

We conducted an unbiased dense core survey in Orion A using the $C^{18}O$ data taken by Nobeyama 45 m telescope. The main conclusions are summarized as follows.

1. The $C^{18}O(J = 1\text{–}0)$ emission is likely to be a reliable tracer of molecular mass toward the regions with $N \lesssim 5 \times 10^{22}\,cm^{-2}$. The average abundance of $C^{18}O$ relative to H_2 is obtained to be 5.7×10^{-7}. This abundance tends to be smaller for the denser region within a factor of a few.
2. Applying Dendrogram, we conducted hierarchical structure analysis of the Orion A cloud and define leaves as cores. As a result, we identified 746 cores. Using the HOPS catalog, we classified the cores into two groups: 709 starless cores and 37 protostellar cores.
3. We derived the masses of the cores identified from the Herschel–Planck H_2 map by removing the contribution of the ambient gas that is not associated with cores along the line of sight.
4. The mean diameter, mass, and velocity widths of the starless cores are estimated to be 0.16 ± 0.05 pc, $0.92 \pm 1.65\,M_\odot$, and $0.32 \pm 0.14\,km\,s^{-1}$, respectively.
4. The CMF of the starless bound cores has a slope similar to the Salpeter IMF in the high-mass part (a power index of $\alpha = -2.24 \pm 0.16$ at $\gtrsim0.44\,M_\odot$) and has a peak at $0.3\,M_\odot$.
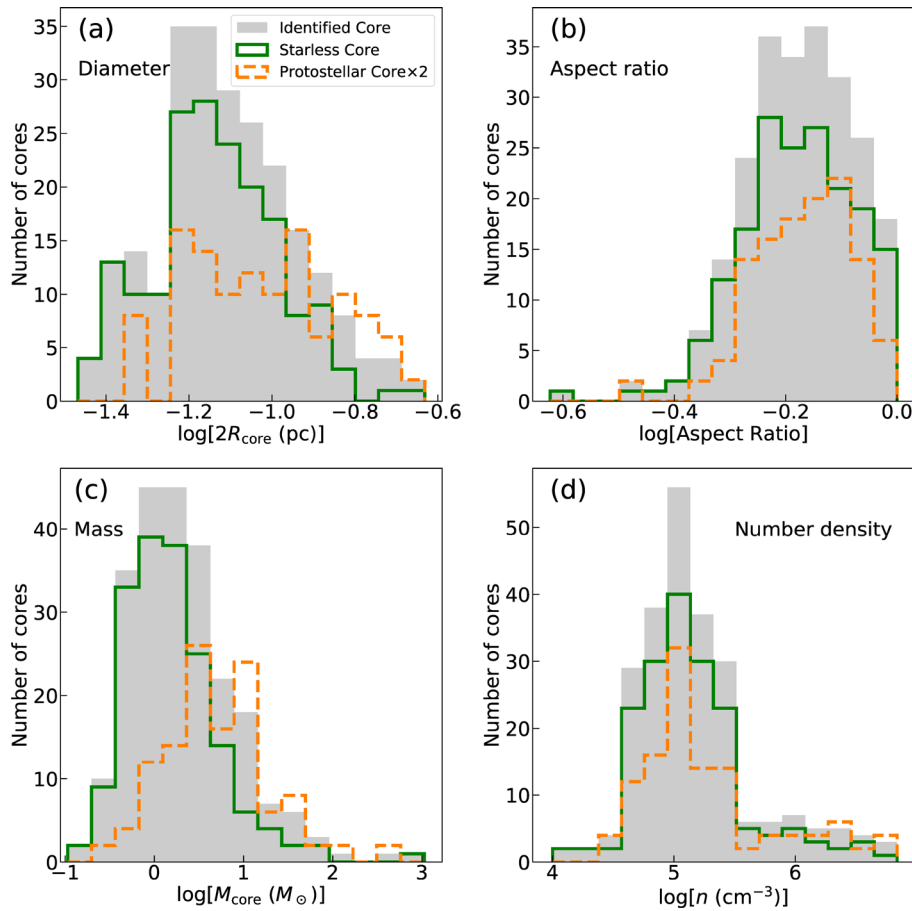
Fig. 12. Histograms of (a) the diameter (b) the aspect ratio, (c) the core mass, and (d) the number density of dust cores. The histogram for the all dust cores is shown in grey. The green and orange histograms are for starless cores and protostellar cores. (Color online)

5. The test of completeness indicates that this peak mass may be affected by the angular resolution of the map, and the actual peak mass, if it exists, would be smaller than the observed value from our data.

6. The estimated mass of cores based on the dust observations is likely to be overestimated the actual core mass, presumably be a factor of ∼3.

7. If we adopt this correction factor for the CMF obtained by Nutter and Ward-Thompson (2007), the peak mass in the CMF tends to be comparable to the stellar IMF.

Supplementary data

The following supplementary data is available at PASJ online.

Complete listing of tables 3 and 4.

Acknowledgments

Appendix 1. H_2 column densities of leaf and trunk with different temperature

In equation (2), we derived core mass with $C^{18}O$ intensity ratio, $I_{C^{18}O, leaf}/I_{C^{18}O, trunk}$ (figure 13), of leaves and trunks by assuming that leaves and trunks have the same temperature and fractional abundance of $C^{18}O$ to H_2. In the real situation, however, cores and ambient gas seem to have different temperatures and fractional abundances, i.e., ambient gas has a higher temperature and larger abundance ratio than
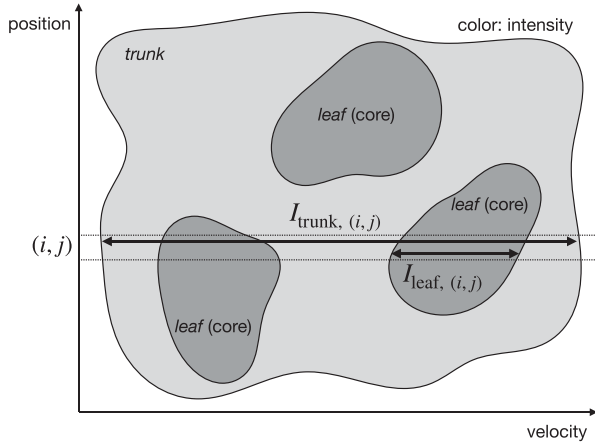
Fig. 13. Schematic representation of how to calculate the core masses using the Herschel–Planck H_2 column density and $C^{18}O$ intensity maps.

cores. In this section, we investigate the influence of such differences on core mass estimation. To do so, we calculate the ratio of H_2 column density of a leaf and trunk from the intensity ratio of leaves and trunks without the assumption that leaves and trunks have the same temperature and fractional abundance using a simple model. First, we fixed the intensity ratio of the leaf and trunk and the temperature of the leaf as $3:7$ (see subsection 5.2) and $20\,K$, respectively. Secondly, we calculated the $C^{18}O$ column density ratio of the leaf and trunk, $N_{C^{18}O, leaf}/N_{C^{18}O, trunk}$, from a temperature range of the trunk of 20 to $100\,K$. Finally, we converted the $C^{18}O$ column density ratio to the H_2

column density ratio, $N_{H_2, leaf}/N_{H_2, trunk}$, with a ratio of fractional abundance ratio, $X_{C^{18}O, trunk}/X_{C^{18}O, leaf}$, of from 1 to 5. Figure 14a shows the relationship between the H_2 column density ratio and the temperature of the trunk. In figure 14b, we normalized the H_2 column density ratio with the intensity ratio. When trunks (ambient gas) have higher temperatures compared to leaves (cores), the H_2 column density ratio, $N_{H_2, leaf}/N_{H_2, trunk}$, is larger than the intensity ratio and we underestimate the core masses. In contrast, when the abundance ratio of a trunk is larger than that of a leaf, the H_2 column density ratio becomes larger. For example, when $T_{trunk} = 40\,K\,(= 2T_{leaf})$ and $X_{C^{18}O, trunk}/X_{C^{18}O, leaf} = 2$, the H_2 column density ratio is similar to the $C^{18}O$ intensity ratio. We expect both effects happen simultaneously in the real situation and we think we can derive the H_2 column density ratio from the $C^{18}O$ intensity ratio of a leaf and a trunk to calculate the core mass with equation (2).

Appendix 2. Overlapping cores

As we mentioned in sub-subsection 4.2.2, around 60% of identified cores overlap each other. In this section, we summarize the properties of overlapped cores such as the number of them, the integrated $C^{18}O$ intensity, and the H_2 column density. Figure 15a shows a histogram of the number of overlapped cores, $N_{overlap}$. For more than 60% of overlapped cores, $N_{overlap} = 1$; several cores have $N_{overlap}$ larger than 3. Figure 15b represents the distributions of overlapped cores in the $I_{C^{18}O}$–$N_{H_2, leaf}$ plane and there is no bias in the distribution. Thus we do not recognize any
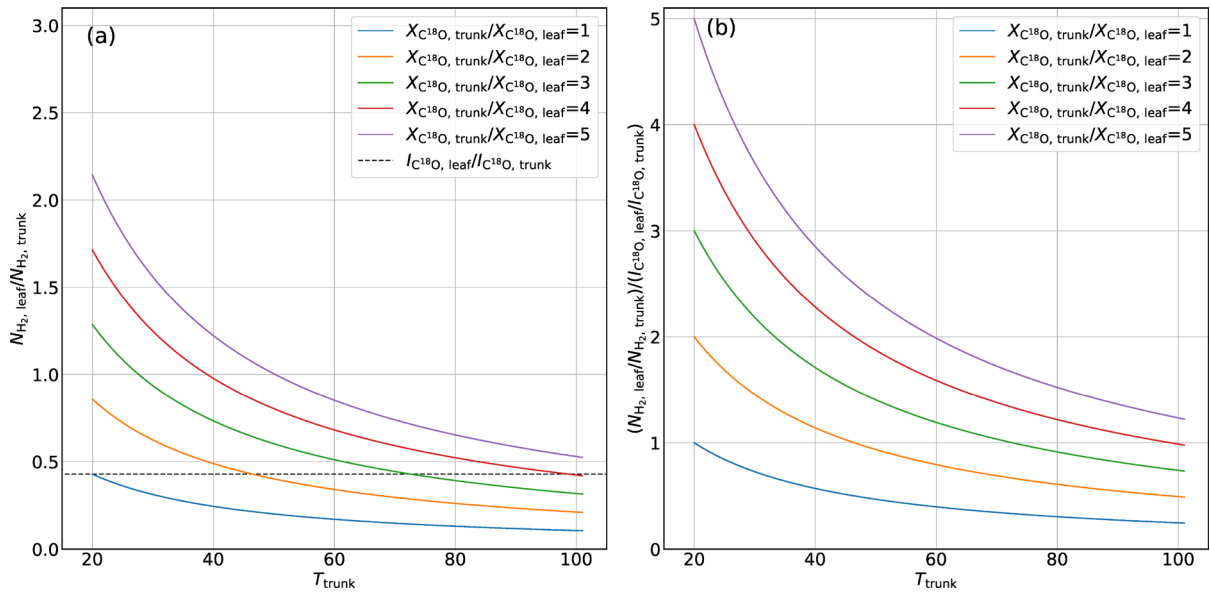
Fig. 14. (a) Relationship between H_2 column density ratio, $N_{H_2, leaf}/N_{H_2, trunk}$ and temperature of trunk with the abundance ratio, $X_{C^{18}O, trunk}/X_{C^{18}O, leaf}$, of form 1 to 5. Here we fix the temperature of leaf and integrated intensity ratio, $I_{C^{18}O, leaf}/I_{C^{18}O, trunk}$, as 20 K and 3/7 (from figure 8), respectively. (b) Relationship between ratio of H_2 column density ratio to integrated intensity ratio and temperature of trunk. (Color online)
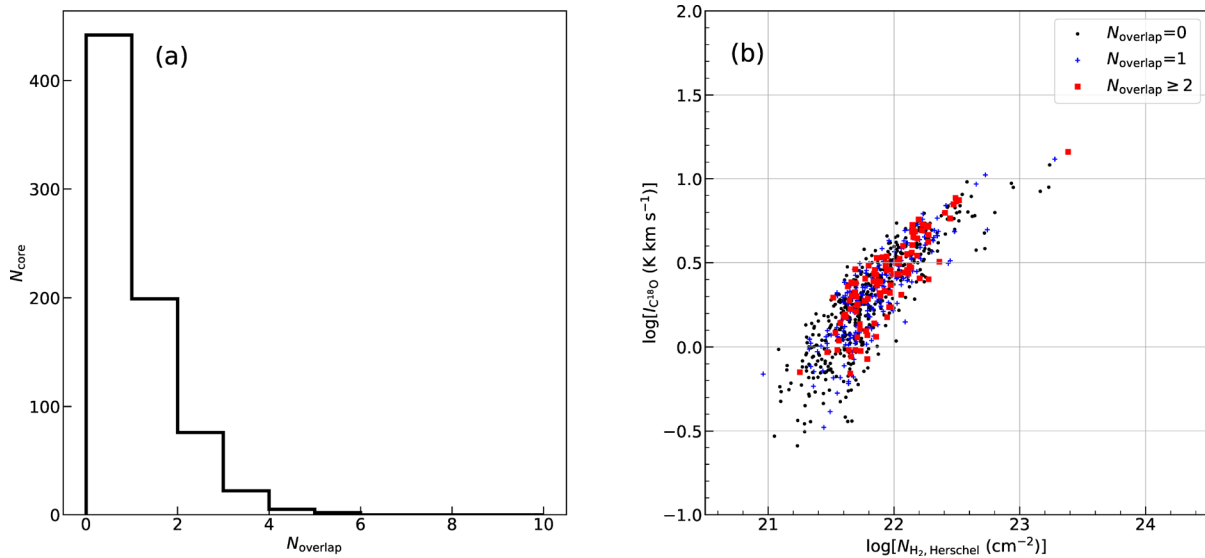
Fig. 15. (a) Histogram of the number of overlapped cores. (b) Distribution of overlapped cores in $I_{C^{18}O}$–$N_{H_2,\,leaf}$ plane. (Color online)

critical integrated intensity or column density at which the overlapping effect becomes severe.

References

Alves, J., Lombardi, M., & Lada, C. J. 2007, A&A, 462, L17

Bally, J., Langer, W. D., Stark, A. A., & Wilson, R. W. 1987, ApJ, 312, L45

Beaumont, C. N., Offner, S. S. R., Shetty, R., Glover, S. C. O., & Goodman, A. A. 2013, ApJ, 777, 173

Bergin, E. A., & Tafalla, M. 2007, ARA&A, 45, 339

Berry, D. S. 2015, Astron. Comput., 10, 22

Bertoldi, F., & McKee, C. F. 1992, ApJ, 395, 140

Bontemps, S., et al. 2001, A&A, 372, 173

Burkhart, B., Lazarian, A., Goodman, A., & Rosolowsky, E. 2013, ApJ, 770, 141

Caselli, P., Walmsley, C. M., Tafalla, M., Dore, L., & Myers, P. C. 1999, ApJ, 523, L165

Cheng, Y., Tan, J. C., Liu, M., Kong, S., Lim, W., Andersen, M., & Da Rio, N. 2018, ApJ, 853, 160

Da Rio, N., Robberto, M., Hillenbrand, L. A., Henning, T., & Stassun, K. G. 2012, ApJ, 748, 14

Feddersen, J. R., et al. 2018, ApJ, 862, 121

Frerking, M. A., Langer, W. D., & Wilson, R. W. 1982, ApJ, 262, 590

Fukui, Y., et al. 2018, ApJ, 859, 166

Furlan, E., et al. 2016, ApJS, 224, 5

Genzel, R., & Stutzki, J. 1989, ARA&A, 27, 41

Goodman, A. A., Rosolowsky, E. W., Borkin, M. A., Foster, J. B., Halle, M., Kauffmann, J., & Pineda, J. E. 2009, Nature, 457, 63

Gratier, P., et al. 2021, A&A, 645, A27

Hacar, A., Alves, J., Tafalla, M., & Goicoechea, J. R. 2017, A&A, 602, L2

Hillenbrand, L. A. 1997, AJ, 113, 1733

Ikeda, N., & Kitamura, Y. 2009, ApJ, 705, L95

Ikeda, N., Sunada, K., & Kitamura, Y. 2007, ApJ, 665, 1194

Ishii, S., Nakamura, F., Shimajiri, Y., Kawabe, R., Tsukagoshi, T., Dobashi, K., & Shimoikura, T. 2019, PASJ, 71, S9

Kong, S. 2019, ApJ, 873, 31

Kong, S., et al. 2018, ApJS, 236, 25

Könyves, V., et al. 2010, A&A, 518, L106

Lada, C. J., Lada, E. A., Clemens, D. P., & Bally, J. 1994, ApJ, 429, 694

Lim, W., et al. 2021, PASJ, 73, S239

Lin, S.-J., et al. 2016, ApJ, 826, 193

Liu, M., Tan, J. C., Cheng, Y., & Kong, S. 2018, ApJ, 862, 105

Lombardi, M., Bouy, H., Alves, J., & Lada, C. J. 2014, A&A, 566, A45

Machida, M. N., & Matsumoto, T. 2012, MNRAS, 421, 588

Maruta, H., Nakamura, F., Nishi, R., Ikeda, N., & Kitamura, Y. 2010, ApJ, 714, 680

Matzner, C. D., & McKee, C. F. 2000, ApJ, 545, 364

Menten, K. M., Reid, M. J., Forbrich, J., & Brunthaler, A. 2007, A&A, 474, 515

Minamidani, T., et al. 2016, Proc. SPIE, 9914, 99141Z

Motte, F., et al. 2018, Nature Astron., 2, 478

Motte, F., Andre, P., & Neri, R. 1998, A&A, 336, 150

Nakamura, F., et al. 2012, ApJ, 746, 25

Nakamura, F., et al. 2019, PASJ, 71, S3

Nutter, D., & Ward-Thompson, D. 2007, MNRAS, 374, 1413

Padoan, P., Pan, L., Juvela, M., Haugbølle, T., & Nordlund, Å. 2020, ApJ, 900, 82

Palla, F., & Stahler, S. W. 1999, ApJ, 525, 772

Pety, J., et al. 2017, A&A, 599, A98

Ripple, F., Heyer, M. H., Gutermuth, R., Snell, R. L., & Brunt, C. M. 2013, MNRAS, 431, 1296

Rosolowsky, E. W., Pineda, J. E., Kauffmann, J., & Goodman, A. A. 2008, ApJ, 679, 1338

Salpeter, E. E. 1955, ApJ, 121, 161

Sanhueza, P., et al. 2019, ApJ, 886, 102

Savva, D., Little, L. T., Phillips, R. R., & Gibb, A. G. 2003, MNRAS, 343, 259

Shimajiri, Y., et al. 2011, PASJ, 63, 105

Shimajiri, Y., et al. 2014, A&A, 564, A68

Shimajiri, Y., et al. 2015, ApJS, 217, 7

Stutz, A. M., & Kainulainen, J. 2015, A&A, 577, L6

Tanabe, Y., et al. 2019, PASJ, 71, S8

Tatematsu, K., Ohashi, S., Sanhueza, P., Nguyen Luong, Q., Umemoto, T., & Mizuno, N. 2016, PASJ, 68, 24

Vázquez-Semadeni, E., Palau, A., Ballesteros-Paredes, J., Gómez, G. C., & Zamora-Avilés, M. 2019, MNRAS, 490, 3061

Williams, J. P., de Geus, E. J., & Blitz, L. 1994, ApJ, 428, 693